Geometries and Terahertz Motions Driving Quintet Multiexcitons and Ultimate Triplet-Triplet Dissociations via the Intramolecular Singlet Fissions

Kobori, Yasuhiro
Fuki, Masaaki
Nakamura, Shunta
Hasobe, Taku

(Citation)
Journal of Physical Chemistry B,124(42):9411-9419

(Issue Date)
2020-10-22

(Resource Type)
journal article

(Version)
Accepted Manuscript

(URL)
https://hdl.handle.net/20.500.14094/90007712

Geometries and Terahertz Motions Driving Quintet Multiexcitons and Ultimate Triplet-Triplet Dissociations via the Intramolecular Singlet-Fissions

Yasuhiro Kobori, [†,¢] Masaaki Fuki, [†,¢] Shunta Nakamura,[¶] and Taku Hasobe,[¶]*

[†] Molecular Photoscience Research Center, Kobe University, 1–1 Rokkodai–cho, Nada–ku, Kobe 657–8501, Japan

[¢] Department of Chemistry, Graduate School of Science, Kobe University, 1–1 Rokkodai–cho, Nada–ku, Kobe 657–8501, Japan

[¶] Department of Chemistry, Faculty of Science and Technology, Keio University, Yokohama, 223-8522, Japan

ABSTRACT: Importance of vibronic effects has been highlighted for the singlet-fission (SF) that convert one high-energy singlet exciton into doubled triplet excitons, as strongly coupled multiexcitons. However, molecular mechanisms of spin conversion processes and ultimate de-couplings in the multiexcitons are poorly understood. We have analyzed geometries and exchange couplings (singlet-quintet energy gaps: 6J) of the photoinduced multiexcitons in the pentacene dimers bridged by a phenylene at ortho and meta positions [denoted as *o*-$(Pc)_2$ and *m*-$(Pc)_2$] by simulations of the time-resolved electron paramagnetic resonance spectra. We clarified that

terahertz molecular conformation dynamics play roles on the spin conversion from the singlet strongly coupled multiexcitons ^{1}(TT) to the quintet multiexcitons ^{5}(TT) and on the intramolecular de-couplings in the 6*J* to form spin correlated triplet pairs (T + T). The strongly coupled ^{5}(TT) multiexcitons are revealed to possess entirely planar conformations stabilized by mutually delocalized spin distributions, while the intramolecular de-coupled spin-correlated triplet pairs generated at 1 μs are also stabilized by distorted conformations resulting in two separately localized biradical characters.

INTRODUCTION

Singlet fission (SF)[1] is expected to exceed the Shockley–Queisser theoretical limit[2] with power conversion efficiencies (PCE) ~33 % of single junction organic solar cells (OSC) because two separated triplet excitons (T+T) can be produced from one excited singlet state (S_1S_0) sharing its excitation energy with a neighboring ground-state chromophore.[3-8] The intramolecular SF (iSF) dynamics have widely been studied using the transient absorption spectroscopic methods together with theoretical modeling taking into account the vibronic effects in the ultrafast regimes.[9-15] The correlated intermolecular triplet pair ^{1}(TT) generated with the singlet character is known to be converted to the quintet (Q) state as ^{5}(TT).[16-25] These TT pairs separate into individual triplets as the T+T state. In the previous study, we reported the iSF dynamics and subsequent separations to T+T in the pentacene dimers (PcD) bridged by a phenylene at ortho and meta positions, as *o*-$(Pc)_2$ and *m*-$(Pc)_2$ in Figure 1 by a combination of the ultrafast transient absorption spectroscopy and the time-resolved electron paramagnetic resonance (TREPR) method.[26] It was concluded that the quintet generations play a major role for suppressing the unwanted loss of the TT to the pair of the ground state (S_0S_0), as the multiexciton recombination process.

Before the spin-conversions to the ^{5}(TT) state, the initially populated ^{1}(TT) is strongly coupled in the four unpaired spins of the two triplet excitons, i.e. the entangled spin-state by large spin-spin exchange coupling (J) with the large orbital overlap produced at femtoseconds regions. The modulations of the J-couplings are thus thought to be essential for the ^{1}(TT) -> ^{5}(TT) conversions.[16-17, 21, 27] The quintet electron spin polarization (ESP) was detected as the microwave absorption (A) and emission (E) in thin films of the SF-materials.[21] The ESPs were interpreted with the sublevel-selective spin conversions by the zero-field splitting (ZFS) interaction in the presence of the negative J during triplet exciton-diffusion and subsequent re-encounter, causing modulation of the J-coupling and the spin decoherences to result in ^{5}(TT).[17, 21] In an iSF system, on the other hand, Kobori and coworkers interpreted that the quintet ESPs were caused by the anisotropic spin conversions due to singlet-quintet spin-relaxations to the five sublevels at m_S = +2, +1, 0, -1 and -2 in accordance with the anisotropy of the ZFS coupling which is highly dependent on the relative orientation of one triplet exciton (T_B) with respect to the other triplet (T_A) in the T_AT_B multiexciton.[20] Internal fluctuations in the J-coupling were concluded to be crucial on the quintet generations. Moreover, we reported the treatment of the EPR transitions in the weakly coupled T+T states in the framework of the spin-correlated triplet pair (SCTP) [22] for the very weak exchange coupling including the superpositions of the nine basis functions of ^{5}(TT) – ^{3}(TT) – ^{1}(TT), as treated in the spin-correlated radical pair model.[28-29]

The above pioneering interpretations of the ESP mechanisms may pave a new avenue to clarify how the molecular conformations and their motions drive the spin-conversions and the ultimate T+T generations, both of which are essential but unknown for the photon-to-energy conversion process. In particular, because the J-coupling is anticipated to be sensitive to the T_AT_B conformations, it is expected that the specific molecular motions or phonon modes may play roles

for the ultimate T+T de-coupling,[30] as the vibronic effects. So far, details of the T_AT_B geometries, the vibration modes and frequencies, and the electronic couplings are unresolved in the iSF systems for generating the quintet multiexcitons and the subsequent T+T dissociations.

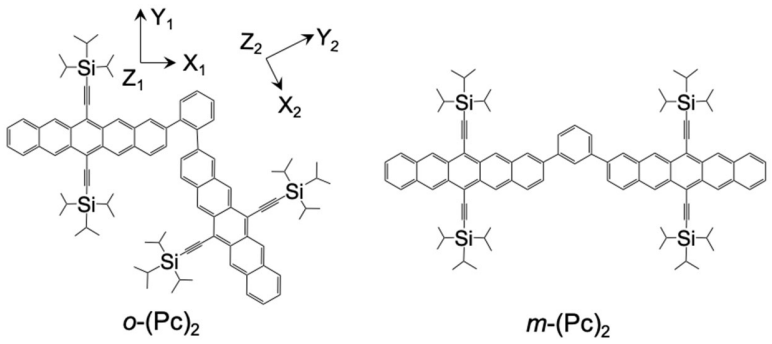

Figure 1. Chemical structures of the pentacene dimers linked by phenylene spacers. Principal axes of the zero-field splitting interactions of the individual triplets are indicated by X_i, Y_i and Z_i. The angle between the Z_1 and Z_2 axes are defined as the dihedral angle of β.

We present a novel theoretical tool to analyze the ESPs of the intramolecular multiexcitons of the quintet state and of the weakly-coupled SCTP state within a framework of the electron spin polarization transfer (ESPT) based upon the stochastic-Liouville equations. We have successfully interpreted the reported TREPR spectra of the multiexcitons observed for the dimers of *o*-$(Pc)_2$ and *m*-$(Pc)_2$ and clarified that terahertz conformational motions plays a role on generating the quintet state and the T+T state.

RESULTS AND DISCUSSION

TREPR Spectra. Figure 2 shows the TREPR spectra of *o*-$(Pc)_2$ and *m*-$(Pc)_2$ at $T = 77$ K in the frozen glass of toluene. The inner components with a peak splitting of ~15 mT as indicated by the blue arrows were assigned to ^{5}(TT) in the previous report.[26] The outer spectrum components

possessing the 41 mT separations indicated by the red arrows were attributed to the T+T state in the dimer of *m*-$(Pc)_2$. According to the anisotropic spin-relaxation model,[20] the spin polarization pattern of the ^{5}(TT) state is highly dependent of the T_AT_B conformation. The difference in the spin polarization pattern in the quintet states between Figure 2a and 2b thus indicates that the conformation of the T_B is different with respect to the conformation of T_A in the multiexcitons.

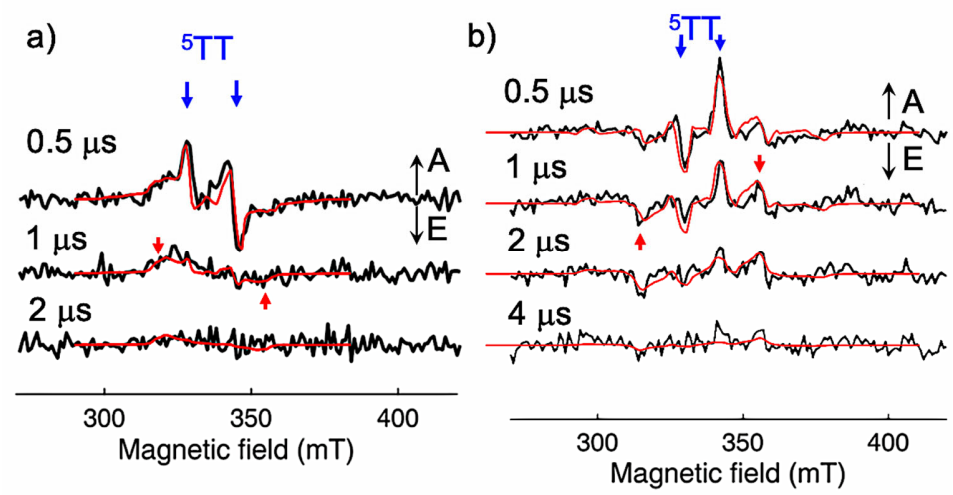

Figure 2. Delay time dependence of the TREPR spectra obtained by the depolarized 532 nm laser irradiation of a) *o*-$(Pc)_2$ and *m*-$(Pc)_2$ at 77 K in the frozen glass of toluene. The red lines are computed TREPR spectra as the sums of the transverse magnetizations, eq.(13) by the quintet TT and the SCTP as the T+T states based on the ESPT model.

Modeling Electron Spin Polarization of the Quintet Multiexcitons. To interpret the delay time dependence of the ESP to gain the detailed molecular mechanisms of the multiexciton dynamics, we now consider three different T_AT_B conformations to numerically compute the spin-state density matrices (ρ_{TT1}, ρ_{TT2} and ρ_{T+T}) of the intramolecular multiexcitons: two of the strongly exchange-coupled multiexcitons (TT_1 and TT_2 states) and one weakly-coupled triplet pair (T+T state) with different potential energies (Figure 3) and with exchange couplings of $6J$ as the singlet-quintet energy gaps in the iSF systems in Figure 4. In Figure 3a, potential energy curves of the

quintet multiexcitons are shown as function of nuclear coordinate. The TT_2 state corresponds to a hot state which is thermally accessible with $\Delta E = 80$ cm^{-1} from the TT_1 state by torsional molecular vibrations, as shown in Figure 3b. Thus, quick molecular conformation changes between the TT_1 and TT_2 states may occur although the TT_1 state is predominantly populated at the cryogenic condition. The T_AT_B conformation of the de-coupled T+T state is assumed to be very different from the strongly coupled TT_1 and TT_2 conformations, resulting in slow dissociation with $k_{DISS} \approx 10^6$ s^{-1} due to a dramatical change in the electronic distribution in Figure 3a, as detailed below.

In the TT_1 state, the primary SF preferentially produces the ^{1}(TT) state, as shown by the red singlet population in Figure 4. The $6J$ value is now assumed to be very strong, as indicated by the dotted red arrow, so that the ^{1}(TT) and the five of the $^5(\mathrm{TT})_{m_S}$ states constitute the diagonalized spin Hamiltonian ($\boldsymbol{H}_{TT} = \boldsymbol{H}_{TTZ} + \boldsymbol{H}_{TTzfs} + \boldsymbol{H}_{TTss} + \boldsymbol{H}_{TTee}$) composed of the Zeeman interaction ($\boldsymbol{H}_{TTZ}$), the ZFS interactions ($\boldsymbol{H}_{TTzfs}$) in the individual triplets, the spin–spin dipolar coupling between the triplets represented by $\boldsymbol{H}_{TTss} = D_{SS}\,(\cos^2\theta_D - 1/3)(3\mathbf{S}_{1Z}\mathbf{S}_{2Z} - \mathbf{S}_1\mathbf{S}_2)$,[22] and the exchange interaction ($\boldsymbol{H}_{TTee} = -2J\,\mathbf{S}_1\mathbf{S}_2$).[21]

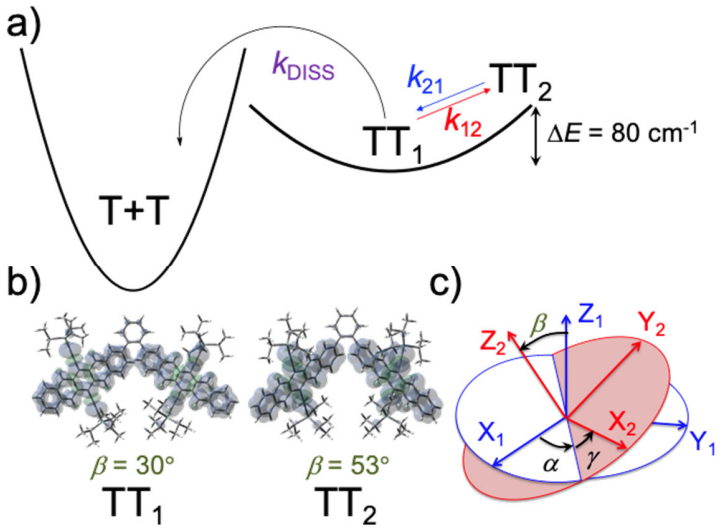

Figure 3. a) Schematic representation of potential energy curves of the multiexcitons as function of nuclear coordinate. b) Geometries of the two strongly coupled multiexcitons to compute the spin sublevel energies in the TT_1 and TT_2 states in Figure 4. TT_2 corresponds a hot state thermally accessible from TT_1 by torsional molecular vibrations to weaken the exchange coupling. The spin density distributions were computed with the B3LYP/3-21G* level molecular orbital calculations for the quintet states. c) Euler angles charactering geometry of the second TIPS-Pentacene group with respect to the other TIPS-Pentacene in the dimer.

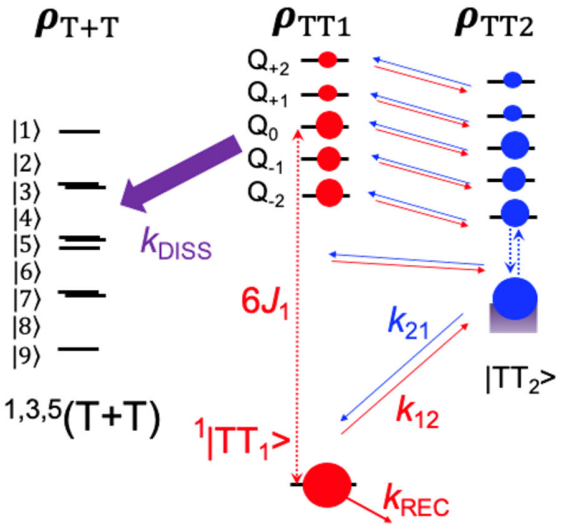

Figure 4. Spin-states of TT_1, TT_2 and T+T. The ^{3}(TT) levels are not shown in TT_1 and TT_2. The density matrix elements of the singlet-quintet systems may rapidly be transferred back and forth

between the TT_1 and the thermally activated TT_2 state through the molecular motions or vibrations including the singlet-quintet coherences. The exchange coupling in the activated TT_2 state may be weaker than in the TT_1 state due to the distorted conformations. The T+T state corresponds the SCTP state with a very weak *J*-coupling.

As for the ^{1}(TT) states, one may treat that this multiexciton partially possesses the singlet charge-transfer (CT) character during the primary SF process by the electronic couplings.[4, 31] Thus, the ^{1}(TT) state energy can be stabilized due to the configuration interaction from the high-lying CT states of $^1Pc^{+\bullet}$-$Pc^{-\bullet}$ and $^1Pc^{-\bullet}$-$Pc^{+\bullet}$ electronic configurations, as reported by Zang et al.[3] The above energy shift of the ^{1}(TT) state is treated as the 6*J* of the singlet-quintet gap,[32] as follows,

$$6J = \frac{|T_{\mathrm{LH}}|^2 + |T_{\mathrm{HL}}|^2}{E_{\mathrm{TT}} - E_{\mathrm{CT}}} \qquad (1)$$

where T_{LH} and T_{HL} represent bridge-mediated $LUMO_A$-$HOMO_B$ and $LUMO_B$-$HOMO_A$ transfer-integrals[26] between the lowest unoccupied molecular orbital (LUMO) and highest occupied molecular orbital (HOMO) in the adjacent monomer units (Pc_A and Pc_B), respectively. E_{TT} and E_{CT} denote the energies of the TT and the CT states. Using $E_{\mathrm{TT}} - E_{\mathrm{CT}} = -4000$ cm^{-1} and $|T_{\mathrm{LH}}| = |T_{\mathrm{HL}}| = 400$ cm^{-1} estimated from the previous cyclic voltammetry (CV) measurements,[3, 26] $J_1 = -220$ GHz is estimated for the TT_1 state in *o*-$(Pc)_2$ from eq.(1). $J_1 = -98$ GHz is assumed in the TT_1 state (Figure 5) for *m*-$(Pc)_2$ because of the weaker chromophore coupling than in *o*-$(Pc)_2$.[26]

In $\boldsymbol{H}_{\mathrm{TTzfs}}$ ($= \mathbf{S}_1\boldsymbol{D}_1\mathbf{S}_1 + \mathbf{S}_2\boldsymbol{D}_2\mathbf{S}_2$), $\mathbf{S}_i$ is the *i*-th triplet spin operator (*i* = 1 and 2 for A and B moieties, respectively in the T_AT_B multiexciton), and $\boldsymbol{D}_i$ represents the ZFS tensor of the individual triplet. The matrix of the $\boldsymbol{H}_{\mathrm{TTzfs}}$ tensor is dependent on the orientation of the principal axes in the $\boldsymbol{D}_2$ tensor (X_2, Y_2, Z_2) with respect to the principal axes in $\boldsymbol{D}_1$ tensor (X_1, Y_1, Z_1), the geometries of the second TIPS-pentacene groups were generated by using Euler rotation angles (α, β, γ) with respect to the

principal axes in $\boldsymbol{D}_i$ as shown in Figure 3c. In particular, it was reported that the quintet ESP is highly dependent of the dihedral angle (β) between the Z_1 and Z_2 axes in the aromatic chromophores in Figure 1.[20] Direction for the second triplet-state position in TT was set by the polar angles (θ_2 and ϕ_2) with respect the (X_1, Y_1, Z_1) principal axes.[22] The direction of the external magnetic field ($\boldsymbol{B}_0$) was set by the polar angles (θ, ϕ).[21] Thus, $\cos^2\theta_D$ where θ_D is the angle between $\boldsymbol{B}_0$ and the inter-spin vector in $\boldsymbol{H}_{TTss} = D_{SS}\ (\cos^2\theta_D - 1/3)(3\mathbf{S}_{1Z}\mathbf{S}_{2Z} - \mathbf{S}_1\mathbf{S}_2)$ is defined for each $\boldsymbol{B}_0$ direction, as reported previously.[33]

The vibronic effect can be treated by setting the three different 6J parameters for the different geometries corresponding to TT_1, TT_2, and T+T in Figure 4. After the rapid primary SF to populate the singlet TT_1 state with the strong J_1, it is anticipated that the β angle between the Pc chromophores is modulated by the molecular motions, as shown in Figure 3b resulting in a weaker J-coupling ($J_2 = -9$ GHz) assumed in the TT_2 state. This weakened J_2 may coincide with $\beta = 53°$ which is larger than $\beta = 30°$ in TT_1, because $|T_{LH}|$ and $|T_{HL}|$ are anticipated to be significantly decreased by slight increases in the edge-to-edge distance and in the orbital orthogonality between the triplet chromophores. This weak J_2 may enable partial instantaneous singlet-quintet interconversions through the anisotropic $\boldsymbol{H}_{TTzfs}$ while such conversions are prohibited in TT_1, as detailed below. Even though the thermally activated TT_2 state immediately returns to the original TT_1, quick repetitive molecular motions eventually induce the singlet-quintet decoherences to produce the anisotropic spin sublevel populations as the red quintet populations in Figure 4, which phenomenon is relevant to the spin-lattice relaxation due to the J-modulations.[34-35] Thus, the combination of (J_2, β) is sensitive both to the spectrum shape and to magnitude of ESP and was chosen to be (–9 GHz, 53°) to fit the delay time dependence of the TREPR data. The respective

quick equilibrium between TT_1 and TT_2 and the T+T dissociation were previously observed by the ultrafast transient spectroscopy.[36] This kinetics is computed by solving the coupled stochastic-Liouville equations, as follows,

$$\dot{\boldsymbol{\rho}}_{\mathrm{TT1}} = -i\left[\widehat{\boldsymbol{H}}_{\mathrm{TT1}}, \boldsymbol{\rho}_{\mathrm{TT1}}\right] - k_{12}\boldsymbol{\rho}_{\mathrm{TT1}} + k_{21}\boldsymbol{\rho}_{\mathrm{TT2}} - k_{\mathrm{DISS}}\boldsymbol{\rho}_{\mathrm{TT1}} + \widehat{\boldsymbol{K}}_{\mathrm{REC}}\boldsymbol{\rho}_{\mathrm{TT1}} \quad (2)$$

$$\dot{\boldsymbol{\rho}}_{\mathrm{TT2}} = -i\left[\widehat{\boldsymbol{H}}_{\mathrm{TT2}}, \boldsymbol{\rho}_{\mathrm{TT2}}\right] + k_{12}\boldsymbol{\rho}_{\mathrm{TT1}} - k_{21}\boldsymbol{\rho}_{\mathrm{TT2}} \quad (3)$$

$$\dot{\boldsymbol{\rho}}_{\mathrm{T+T}} = -i\left[\widehat{\boldsymbol{H}}_{\mathrm{T+T}}, \boldsymbol{\rho}_{\mathrm{T+T}}\right] + k_{\mathrm{DISS}}\boldsymbol{\rho}_{\mathrm{TT1}} + \widehat{\boldsymbol{K}}_{2}\boldsymbol{\rho}_{\mathrm{T+T}} \quad (4)$$

In eqs (2)-(4), five of the ${}^5(\mathrm{TT})_{m_S}$ – ${}^1(\mathrm{TT})$ two-level interconversions are separately treated among the nine basis functions (singlet, triplets and quintets) that diagonalize $\widehat{\boldsymbol{H}}_{\mathrm{TT1}}$ in the presence of J_1 assuming that the spin-conversions within the quintet levels and the conversions from ${}^5(\mathrm{TT})$ to ${}^3(\mathrm{TT})$ are ignored because the ${}^1(\mathrm{TT})$ –> ${}^5(\mathrm{TT})$ conversions are initially predominant through $\boldsymbol{H}_{\mathrm{TTzfs}}$. $\widehat{\boldsymbol{K}}_{\mathrm{i}}\boldsymbol{\rho} = -k_{\mathrm{i}}(|\mathrm{S}\rangle\langle\mathrm{S}|\boldsymbol{\rho} + \boldsymbol{\rho}|\mathrm{S}\rangle\langle\mathrm{S}|)/2$ is substituted as the singlet deactivation by ${}^1(\mathrm{TT}) \rightarrow (S_0S_0)$ in eqs.(2) and (4).[37] Therefore, from eqs.(2)-(4), the time dependence of the twelve elements, ρ_{SS1}, ρ_{SQ1}, ρ_{QS1}, ρ_{QQ1}, ρ_{SS2}, ρ_{SQ2}, ρ_{QS2}, ρ_{QQ2}, $\rho_{\mathrm{SS(T+T)}}$, $\rho_{\mathrm{SQ(T+T)}}$, $\rho_{\mathrm{QS(T+T)}}$, and $\rho_{\mathrm{QQ(T+T)}}$ where S = ${}^1(\mathrm{TT})$ and Q = ${}^5(\mathrm{TT})_{m_S}$ are solved using a matrix form of the time-differential equation of $\partial\vec{\boldsymbol{\rho}}/\partial t = \boldsymbol{L}\vec{\boldsymbol{\rho}}$, as detailed in eqs.(S1)-(S7) and Table S1 of the Supporting Information. The time developments of the density matrix elements in $\vec{\boldsymbol{\rho}}$ are thus computed by the following equation:[38]

$$\vec{\boldsymbol{\rho}}(t) = \boldsymbol{S}_{\mathrm{TT}} exp(\boldsymbol{\eta}t)\boldsymbol{S}_{\mathrm{TT}}^{-1}\vec{\boldsymbol{\rho}}(t=0) \quad (5)$$

where $\boldsymbol{S}_{\mathrm{TT}}$ and $\boldsymbol{\eta}$ are the eigenvectors and the eigenvalues matrices obtained by diagonalizing the $\boldsymbol{L}$ matrices[33] in Table S1 with $\rho_{\mathrm{SS1}}(t = 0) = 1$ and with the other terms being zeros as the initial condition.

From eqs. (2), (3) and (5), the time developments of the transverse magnetizations of ρ_{m_S,m_S-1} (m_S =+2, +1, 0, and –1) are computed both for the ^{5}TT$_1$ and ^{5}TT$_2$ states with $S = 2$ under the very weak microwave strength (ω_1) in the rotating frame,[39] as follows,

$$\begin{pmatrix}\rho^{\mathrm{TT1}}_{m_S,m_S-1}\\ \rho^{\mathrm{TT2}}_{m_S,m_S-1}\end{pmatrix} = \omega_1 \begin{pmatrix} -\left(-\omega_0 + E^{\mathrm{TT1}}_{\mathrm{Q}m_S} - E^{\mathrm{TT1}}_{\mathrm{Q}m_S-1}\right) + i\left(k_{12} + \frac{1}{T_{2\mathrm{Q}}}\right) & -ik_{21} \\ -ik_{12} & -\left(-\omega_0 + E^{\mathrm{TT2}}_{\mathrm{Q}m_S} - E^{\mathrm{TT2}}_{\mathrm{Q}m_S-1}\right) + i\left(k_{21} + \frac{1}{T_{2\mathrm{Q}}}\right) \end{pmatrix}^{-1} \times$$

$$\begin{pmatrix}\rho^{\mathrm{TT1}}_{m_Sm_S} - \rho^{\mathrm{TT1}}_{m_S-1,m_S-1}\\ \rho^{\mathrm{TT2}}_{m_Sm_S} - \rho^{\mathrm{TT2}}_{m_S-1,m_S-1}\end{pmatrix}\{S(S+1) - m_S(m_S-1)\} \qquad (6)$$

where ω_0, $E^{\mathrm{TT1}}_{\mathrm{Q}m_S}$ and $E^{\mathrm{TT2}}_{\mathrm{Q}m_S}$ represent the microwave energy, the eigenenergies of the quintet sublevels in the respective TT$_1$ and TT$_2$ states in the units of angular frequencies. $T_{2\mathrm{Q}}$ denotes the phase memory time. Thus, the present EPR line-shape analysis reflects the dynamics on the sublevel populations and on the motional-narrowing effect between the two different quintet conformations caused by the quick nuclear motions or vibrations. From ΔE in Figure 3a, the following relation is utilized for the inter-exchange process between TT$_1$ and TT$_2$:

$$k_{12} = k_{21}e^{-\frac{\Delta E}{k_BT}} \qquad (7)$$

where ΔE = 80 cm^{-1} was assumed in the present analysis. By the vibration motions in Figure 3a, singlet populations of TT$_1$ and TT$_2$ quickly reach an equilibrium, although the quintet-state populations occur at later time. This quick equilibration time (τ) must be relevant to dephasing time of the molecular vibration, when one treats the k_{12} and k_{21} kinetics to represent the vibration motions. One may now reasonably assume that the dephasing time of the coherent vibration is originating from the variations in the vibration frequencies, and thereby that such inhomogeneity

of the frequency equals to the peak position of the vibration frequencies, as observed by a terahertz spectroscopy.[40] Therefore, the relaxation time τ to reach the $TT_1 \rightleftharpoons TT_2$ equilibrium may be represented by a wavelength ($\bar{\nu}_{\mathrm{vib}}$) of the vibration motion in the present model, as follows,

$$\tau = \frac{1}{k_{12}+k_{21}} = \frac{1}{2\pi c\bar{\nu}_{\mathrm{vib}}} \quad (8)$$

where c represents the speed of light. From eqs. (7) and (8), the vibration motions (k_{12} and k_{21}) are characterized by a single parameter of $\bar{\nu}_{\mathrm{vib}}$.

Modeling Electron Spin Polarization of the T+T Multiexcitons. We recently reported the treatment of the EPR transitions of the weakly coupled T+T states by the SCTP model.[22] The nine spin eigenfunctions were obtained in the presence of the Zeeman interaction and of the ZFS interactions of the triplet excitons to obtain the quintet, triplet and singlet TT states for the very strong J, represented as ${}^5|\mathrm{TT}\rangle_{+2+1,0,-1,-2}$, ${}^3|\mathrm{TT}\rangle_{+1,0,-1}$ and ${}^1|\mathrm{TT}\rangle$.[21] When the exchange coupling is weaker than $\boldsymbol{H}_{\mathrm{TTzfs}}$, on the other hand, the superpositions[22] will occur through $\boldsymbol{H}_{\mathrm{TTzfs}}$ to result in different nine eigenlevels of $|i\rangle$ = 1, 2, ⋯, 9 in Figure 4. For examples, $|i\rangle = |2\rangle$ and $|3\rangle$ are generated by the superpositions of ${}^5|\mathrm{TT}\rangle_{+1}$ and ${}^3|\mathrm{TT}\rangle_{+1}$, while $|i\rangle = |4\rangle, |5\rangle$ and $|6\rangle$ are also obtained by the hybridization of ${}^5|\mathrm{TT}\rangle_0$, ${}^3|\mathrm{TT}\rangle_0$ and ${}^1|\mathrm{TT}\rangle$ due to $\boldsymbol{H}_{\mathrm{TTzfs}}$ for the very weak exchange coupling. These eigenfunctions in ^{1,3,5}(T+T) are computed by diagonalizing $\widehat{\boldsymbol{H}}_{\mathrm{T+T}}$ in eq.(4):

$$\begin{pmatrix} \varepsilon_1 & & \\ & \varepsilon_2 & \\ & & \ddots \end{pmatrix} = \boldsymbol{U}^t_{\mathrm{T+T}}\widehat{\boldsymbol{H}}_{\mathrm{T+T}}\boldsymbol{U}_{\mathrm{T+T}} \quad (9)$$

where ε_i represent nine eigenenegies of $|i\rangle$ in T+T. The transformation matrix is described as,

$$\boldsymbol{U}_{\mathrm{T+T}}=\begin{pmatrix} c_{11} & c_{21} & c_{31} & c_{41} & c_{51} & c_{61} & c_{71} & c_{81} & c_{91} \\ c_{12} & c_{22} & c_{32} & c_{42} & c_{52} & c_{62} & c_{72} & c_{82} & c_{92} \\ c_{13} & c_{23} & c_{33} & c_{43} & c_{53} & c_{63} & c_{73} & c_{83} & c_{93} \\ c_{14} & c_{24} & c_{34} & c_{44} & c_{54} & c_{64} & c_{74} & c_{84} & c_{94} \\ c_{15} & c_{25} & c_{35} & c_{45} & c_{55} & c_{65} & c_{75} & c_{85} & c_{95} \\ c_{16} & c_{26} & c_{36} & c_{46} & c_{56} & c_{66} & c_{76} & c_{86} & c_{96} \\ c_{17} & c_{27} & c_{37} & c_{47} & c_{57} & c_{67} & c_{77} & c_{87} & c_{97} \\ c_{18} & c_{28} & c_{38} & c_{48} & c_{58} & c_{68} & c_{78} & c_{88} & c_{98} \\ c_{19} & c_{29} & c_{39} & c_{49} & c_{59} & c_{69} & c_{79} & c_{89} & c_{99} \end{pmatrix} \quad (10)$$

with $|i\rangle = \sum_j^9 c_{ij}\,|\mathrm{TT}\rangle_j$ where $|\mathrm{TT}\rangle_{1,\cdots 5}$ corresponds to ${}^5|\mathrm{TT}\rangle_{+2,\cdots,-2}$. $|\mathrm{TT}\rangle_{6,7,8}$ corresponds to ${}^3|\mathrm{TT}\rangle_{+1,0,-1}$. And, $|\mathrm{TT}\rangle_9$ equals to ${}^1|\mathrm{TT}\rangle$. The spin-state populations ($\rho^{\mathrm{T+T}}{}_{\mathrm{ii}}$) where i = 1, 2, ⋯, 9 in Figure 4 for the dissociated multiexciton is computed by $\boldsymbol{\rho}_{1-9}^{\mathrm{T+T}} = \boldsymbol{U}_{\mathrm{T+T}}^{t}\boldsymbol{\rho}^{\mathrm{T+T}}\boldsymbol{U}_{\mathrm{T+T}}$, as detailed in eq(S8). The transverse magnetization of the SCTP was obtained as a function of the external magnetic field strength, as,[22]

$$imag(\rho_{i,k}^{\mathrm{T+T}}) = Int(i,k)\frac{\omega_1(\rho_{ii}^{\mathrm{T+T}}-\rho_{kk}^{\mathrm{T+T}})T_2}{1+(\varepsilon_i-\varepsilon_k-\omega_0)^2T_2^2} \quad (11)$$

with, k = 1, 2, ⋯, 9 and

$$Int(i,k) = 4|c_{i1}|^2|c_{k2}|^2 + 4|c_{i2}|^2|c_{k1}|^2 + 6|c_{i2}|^2|c_{k3}|^2 + 6|c_{i3}|^2|c_{k2}|^2 + 6|c_{i3}|^2|c_{k4}|^2 + 6|c_{i4}|^2|c_{k3}|^2 + 4|c_{i4}|^2|c_{k5}|^2 + 4|c_{i5}|^2|c_{k4}|^2 + 2|c_{i6}|^2|c_{k7}|^2 + 2|c_{i7}|^2|c_{k6}|^2 + 2|c_{i7}|^2|c_{k8}|^2 + 2|c_{i8}|^2|c_{k7}|^2 \quad (12)$$

The computations of the time-dependences of the twelve elements, ρ_{SS1}, ρ_{SQ1}, ρ_{QS1}, ρ_{QQ1}, ρ_{SS2}, ρ_{SQ2}, ρ_{QS2}, ρ_{QQ2}, $\rho_{\mathrm{SS(T+T)}}$, $\rho_{\mathrm{SQ(T+T)}}$, $\rho_{\mathrm{QS(T+T)}}$, and $\rho_{\mathrm{QQ(T+T)}}$ were performed for m_{S} = +2, +1, 0, –1, and –2 by eq.(5). One may then obtain the TREPR line-shape function (*SP*) from the eqs.(6) and (11), as follows,

$$SP = -imag\left\{\sum_{m_{\mathrm{S}}}\left(\rho_{m_{\mathrm{S}},m_{\mathrm{S}}-1}^{\mathrm{TT1}} + \rho_{m_{\mathrm{S}},m_{\mathrm{S}}-1}^{\mathrm{TT2}}\right) + \sum_{i\neq k}\rho_{i,k}^{\mathrm{T+T}}\right\} \quad (13)$$

In the second term of eq.(13), sixteen of allowed $i \leftrightarrow k$ transitions ($|1\rangle \leftrightarrow |2\rangle$,$|1\rangle \leftrightarrow |3\rangle$, $|2\rangle \leftrightarrow |4\rangle$, $|2\rangle \leftrightarrow |5\rangle$, $|2\rangle \leftrightarrow |6\rangle$, $|3\rangle \leftrightarrow |4\rangle$, $|3\rangle \leftrightarrow |5\rangle$, $|3\rangle \leftrightarrow |6\rangle$, $|4\rangle \leftrightarrow |7\rangle$, $|4\rangle \leftrightarrow |8\rangle$, $|5\rangle \leftrightarrow |7\rangle$, $|5\rangle \leftrightarrow |8\rangle$, $|6\rangle \leftrightarrow |7\rangle$, $|6\rangle \leftrightarrow |8\rangle$, $|7\rangle \leftrightarrow |9\rangle$, and $|8\rangle \leftrightarrow |9\rangle$ in Figure 4) may contribute between the eigenfunctions for small J. The powder-pattern integrations of eq.(13) were performed to compute the delay time dependences of the spin polarization patterns as the TREPR spectra (the red lines in Figure 2). Decompositions to the components of the quintet states, $-imag(\rho^{\mathrm{TT1}}_{m_S,m_S-1} + \rho^{\mathrm{TT2}}_{m_S,m_S-1})$ and the T+T state of $-imag(\rho^{\mathrm{T+T}}_{i,k})$ in eq.(13) are shown in Figure S1.

Geometries and Motions of the Quintet Multiexcitons. On the fitting of the TREPR spectra, we first estimated the T_AT_B conformation of the multiexcitons in $\boldsymbol{H}_{\mathrm{TTzfs}}$ for the TT1 and TT2 states by the Euler rotation angles (α, β, γ) because the spin polarization pattern is highly dependent on this orientation of the $\boldsymbol{D}_2$ tensor, as reported previously.[20] In *o*-$(Pc)_2$, the strong chromophore interaction was described as mentioned above, resulting in terahertz range of the $6J_1$ parameter from eq.(1). This may cause planarly folded T_AT_B dimer conformation in the TT_1 state resulting in the small β value ($\beta = 30°$) in Figure 3b. On the other hand, $\beta > 30°$ is anticipated for the transition state (TT_2) with ΔE = 80 cm^{-1} in eq.(7), as shown by $\beta = 53°$ in Figure 3b, because the orbital overlap is expected to become weaker (J_2 = –10 GHz). Because such butterfly molecular motions are expected to be quicker than picosecond regime, $\bar{\nu}_{\mathrm{vib}}$ = 26 cm^{-1} was considered. In Figure 2a, the quintet state EPR signal immediately disappeared. With this the very weak broad EPR contribution originating from the T+T state became dominant at 1 μs. Therefore, k_{DISS} = 1.1×10^6 s^{-1} and k_{REC} = 3.0×10^7 s^{-1} were utilized to fit the TREPR spectra.

In *m*-$(Pc)_2$, the chromophore interaction is reported to be weaker than in *o*-$(Pc)_2$.[26] Thus, it is anticipated that the T_AT_B dimer conformation is more flexible in *m*-$(Pc)_2$ than in *o*-$(Pc)_2$. From this,

a planarly extended T_AT_B conformation with $\beta = 22°$ is considered for the TT_1 state, while T_B aromatic plane is assumed to be rotated by the dihedral angle of $\beta = 75°$ with respect to T_A in the TT_2 transition state in *m*-$(Pc)_2$ with $\bar{\nu}_{vib}$ = 72 cm^{-1}, as shown in Figure 5. $k_{DISS} = 1.0\times10^6$ s^{-1} and $k_{REC} = 3.0\times10^6$ s^{-1} were utilized to explain the delay time dependence of the EPR spectra in Figure 2b. The slower singlet recombination kinetics in *m*-$(Pc)_2$ is essential to explain the longer-lived quintet signals in Figure 2b than in Figure 2a. Table S2 summarizes full of applied EPR parameters for computations of the delay time dependences of the EPR spectra (Figure 2).

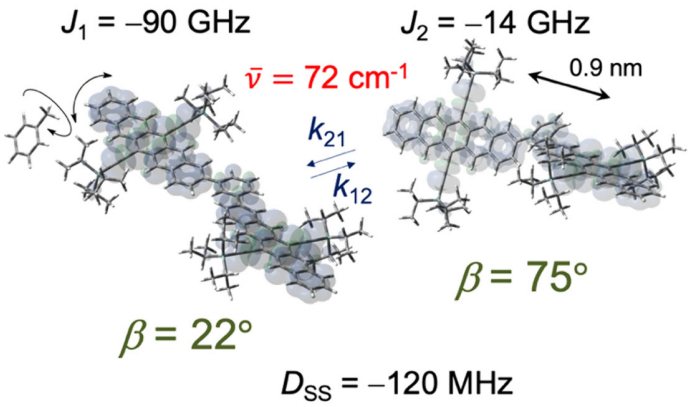

Figure 5. Geometry fluctuation model of the quintet multiexcitons to compute the spin dynamics between the TT_1 (left) and TT_2 (right) states in *m*-$(Pc)_2$ to reproduce the TREPR spectra in Figure 2b. D_{SS} = –120 MHz was utilized representing the inter-spin separations of 0.9 nm in T_AT_B. Internal rotations of the methyl groups of the surrounding solvent molecules would couple to the conformation changes with $\bar{\nu}_{vib}$ = 72 cm^{-1} at 77 K. The delocalized spin density distributions were identified by the weakened $\boldsymbol{H}_{TTzfs}$ in Table S2.

Validities of the ESP in the Quintet Multiexcitons. To validate the quintet EPR transition schemes by the present model in Figure 5, we computed matrix elements of the magnitude of the spin Hamiltonian [abs($\boldsymbol{H}_{TT2}$)] in Table S3 for a specific $\boldsymbol{B}_0$ direction of (θ, ϕ) = (90°,43°) in the (X_1, Y_1, Z_1) coordinate in *m*-$(Pc)_2$. The sizes of the $\langle {}^5TT_{m_S}|\boldsymbol{H}_{TT2}|{}^1TT\rangle$ interactions were in a range of 10^9 rad/s and was strongest for populating the $m_S = 0$ state. This interaction is compatible

with the size of the $\boldsymbol{H}_{\mathrm{TTzfs}}$ interaction of the excited triplet states. We also computed the resultant spin sublevel populations for the TT_1 state at $t = 0.5$ μs, as shown in Figure S2 and confirmed that the quintet populations ρ_{m_S,m_S} are proportional to $\left\langle {}^5\mathrm{TT}_{m_S}\middle|\boldsymbol{H}_{\mathrm{TT2}}\middle|{}^1\mathrm{TT}\right\rangle^2$. The sizes of the spin magnetizations ($\rho_{00} - \rho_{\pm1\pm1}$) exceeding 1.4 % for the Q_0– $\mathrm{Q}_{\pm1}$ transitions in eq.(6) were obtained (Figure S2) and were greater than the thermal equilibrium spin magnetization of $g\beta B_0/2k_{\mathrm{B}}T$ = 0.0028 for the doublet. This strongly indicates that the quintet ESP is detectable by the TREPR method; the significant amount of the quintet population (4.8 %) occurs from the singlet TT_1 (15.6%) with the anisotropic spin-relaxation effects driven by the quick molecular vibrations, although the singlet-quintet energy gaps are larger than the size of $\left\langle {}^5\mathrm{TT}_0\middle|\boldsymbol{H}_{\mathrm{TT2}}\middle|{}^1\mathrm{TT}\right\rangle$ in Table S3.

Geometries of the T+T Multiexcitons. For the de-couplings in the intramolecular multiexcitons to generate the T+T state, it is essential that the 6*J* become significantly weak. Thus, it is highly anticipated that dramatical geometry changes are required to result in the T+T states to reduce both the through-bond and the through-space orbital overlaps ($|T_{\mathrm{LH}}|$ and $|T_{\mathrm{HL}}|$) in eq.(1). From this we propose that the one or both of the Pc units take conformations that the X_i–Y_i planes in $\mathrm{T_A}$ or $\mathrm{T_B}$ in Figure 1 are orthogonal to the aromatic planes of the phenylene spacers of the dimers to minimize the superexchange couplings in $|T_{\mathrm{LH}}|$ and $|T_{\mathrm{HL}}|$ as shown in Figure 6. At the bottom of Figure 6, the SCTP spectra were computed by the corresponding geometries and exchange couplings, exhibiting that the ESP is highly affected by the $\mathrm{T_AT_B}$ conformation. Notably, the absorptive and emissive polarization around 320 mT at 1 μs, as shown by the red arrows in Figure 2a and 2b, respectively, are both consistent with the modulation of the A and E polarizations in Figure 6 around 320 mT. This strongly supports that the large degrees of the $\mathrm{T_AT_B}$ conformation changes in Figure 6 accompany to the intramolecular de-coupling for the T+T state from the planar

T_AT_B geometries in the strongly coupled multiexcitons of TT_1 in Figure 3b. One might hypothesize that solute complex formations or aggregates could induce the T+T separations by the triplet-triplet energy transfers of $T_1T_1 + S_0S_0 \rightarrow T_1S_0 + S_0T_1$. This triplet separation is however excluded because the solute concentrations (50 μM) were very low; no complex formations were conclusive in toluene for the cryogenic temperature at the concentrations of 100 μM for TIPS-pentacene.[21] Furthermore, the exergonic intramolecular T+T dissociations have well been characterized in the previous report by the triplet quantum yield exceeding 100 % in *m*-$(Pc)_2$.[26]

Nature of the Terahertz Conformation Dynamics. As have been discussed previously,[16-17, 21, 27] the fluctuations of the *J*-coupling are essential for generating the quintet multiexcitons. The present model calculations demonstrate that the intramolecular twisting T_AT_B conformation changes are linked to the fluctuations. Importantly, the terahertz vibrations with $\bar{\nu}_{\mathrm{vib}}$ = 26 and 72 cm^{-1} in Figures 3 and 5, respectively, are revealed be crucial to obtain the good agreements with the delay time dependences of the EPR spectra in Figure 2, because the spin-relaxation effects are dependent of the fluctuation frequency.[34] This also coincides with the estimated terahertz range of the $6J_1$ parameter in the TT_1 state from eq.(1) because the spin-lattice relaxation generating $^5(TT)$ is anticipated to be efficient when the 6*J* energy difference between TT_1 and TT_2 roughly resonate with the frequency of the *J*-modulation.[20]

One may raise next questions about origins of the large degrees of the TT conformation changes as in Figure 5 and also in Figure 6 for the T+T dissociations, even though the multiexcitons are dissolved in the bulk frozen solutions. Inherent gas phase low-frequency molecular vibrations must be small and hindered by the surrounding toluene molecules in Figure 5. Instead, the solvent dynamics[20] may cause the terahertz orientation motions. It is well known that the methyl group of

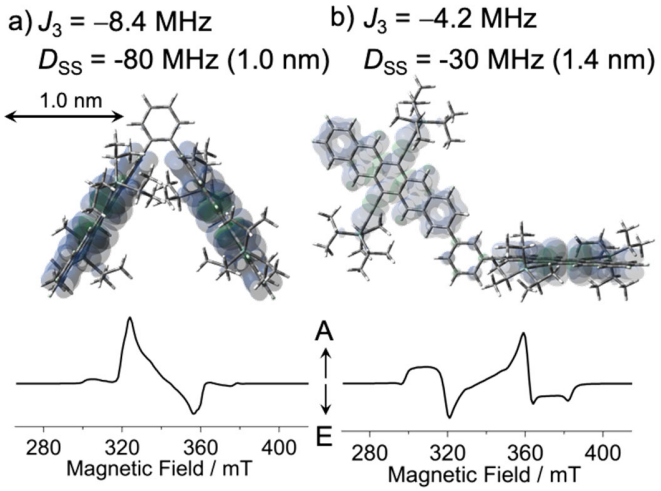

Figure 6. The geometries, exchange-couplings and spin-dipolar couplings of the T+T multiexcitons in a) *o*-$(Pc)_2$ and in b) *m*-$(Pc)_2$, respectively. The parentheses denote inter-spin separations estimated by the point-dipole approximation. Corresponding computed TREPR spectra of the T+T contribution were obtained from the geometries for 1 μs, as shown at the bottom.

toluene undergoes the internal rotation in the cryogenic conditions. Tsukushi et al.[41] characterized the molecular motions of the glass matrix of toluene at cryogenic temperature and reported that 80 cm^{-1} mode of the vibration originates from the internal rotations. This wavenumber well coincides with $\bar{\nu}_{vib}$ = 26 and 72 cm^{-1} and may trigger the conformation dynamics, as shown in Figure 5. In addition, several methyl groups are substituted in the terminal substituents in PcD and may assist the conformation dynamics in *o*-$(Pc)_2$ in Figure 3b, because the internal rotations of the bulky triisopropylsilylethynyl groups near the adjacent Pc moiety would probably affect the electronic coupling within the dimer.[26]

CONCLUSION

We have characterized the molecular geometries, conformation dynamics and exchange couplings of the intramolecular multiexcitons at T = 77 K after the photoinduced iSF with the

proposal of the density matrix analysis of ESP observed by the TREPR method. It is concluded that the terahertz twisting T_AT_B conformation dynamics plays a significant role for generating the quintet multiexcitons and for the individual T+T states in the covalently linked systems.

In the TT_1 states with the very strong J couplings, the T_AT_B takes on the planar conformations (Figure 3b and 5) so that the orbital overlap in T_AT_B is significant. These flat conformations are consistent with a recent ultrafast study of an iSF system; Korovina et al. reported that the initial ^{1}(TT) state conformation possesses the long-range planar structure in the perylene oligomers linked by 1,4-dialkynyl-2,5-bis(ethylhexyloxy)-benzene molecular motif, reflecting electronic delocalized character in the S_1 state.[30] This denotes that the strongly-coupled ^{5}(TT)s also take on the initial ^{1}(TT) flat conformations, most likely because the two triplets in the multiexciton are mutually delocalized in the entire planar geometry in Figure 5 to stabilize the multiexcitons rather than in the twisted conformers of TT_2. The above delocalized feature is very consistent with the weaker ZFS parameters of the D and E values applied in $\boldsymbol{H}_{TTzfs}$ than in the T+T states, as shown in Table S2 to explain the line-shapes of Figure 2. The weakened ZFS interaction is well known for the delocalized triplet spins in the special pair of *Rhodobacter sphaeroides* R26 of the photosynthetic reaction center.[33, 42] These delocalized spin distributions are also compatible with the bridge-mediated CT mechanism of eq.(1) resulting in the negative J rather than the J-coupling mechanism via the nearest neighbor C-C bonds in the phenylene spacer,[43] with which ferromagnetic couplings were predicted by the linkages at the meta positions (Figure 1 right).

It was also clarified, in the T+T dissociations, that the large degrees of the conformation changes occurred with $k_{DISS} \approx 10^6$ s^{-1} (Figure 6). This is also in line with the reported proposal that the torsional disorders resulted to form the two separated triplet excitons in the linked perylene oligomers.[30] After such large degrees of the distortions in Figure 6, the two triplet spins can

separately be localized to form the biradical characters concentrated around the C6 and C13 positions in the pentacene units stabilizing the T+T individual two spins with the significantly reduced orbital overlap.[13] The ultimate T+T dissociations were very slow with respect to the dissociation kinetics of picosecond regime in the crystalline TIPS-pentacene.[8, 22, 44-45] The present small k_{DISS} values are explained by large barriers for the internal conformation changes (Figure 6) associated with the rearrangements of the spin densities to reduce the *J*-decoupling. The present molecular level analysis of the spin-state populations in the multiexciton are thus significantly informative for future designs of the doubled photon-to-energy conversion materials by optimizing the conformation changes and the electronic couplings in the transient multiexcitons including the usage for the four-qubit quantum computing processing initiated by the photon.[22]

ASSOCIATED CONTENT

Supporting Information

The Supporting Information is available free of charge on the ACS Publications website.

Electron spin polarization transfer model for the numerical simulation of the TREPR spectra with the matrix form in Table S1. The full sets of the EPR parameters (Table S2) and the decomposed quintet and the SCTP spectra are detailed in Figure S1. Matrix elements of the magnitudes of the spin Hamiltonian (Table S3) and sublevel populations of the strongly coupled multiexciton (Figure S2) are shown. (PDF)

AUTHOR INFORMATION

Corresponding Author

Yasuhiro Kobori *–Molecular Photoscience Research Center, & Department of Chemistry, Graduate School of Science, Kobe University, 1–1 Rokkodai–cho, Nada–ku, Kobe 657–8501, Japan;* orcid.org/0000-0001-8370-9362; Phone: +81-78-803-6548; E-mail: ykobori@kitty.kobe-u.ac.jp

Authors

Masaaki Fuki*–Molecular Photoscience Research Center, & Department of Chemistry, Graduate School of Science, Kobe University, 1–1 Rokkodai–cho, Nada–ku, Kobe 657–8501, Japan*

Shunta Nakamura*–Department of Chemistry, Faculty of Science and Technology, Keio University, Yokohama, 223-8522, Japan*

Taku Hasobe *–Department of Chemistry, Faculty of Science and Technology, Keio University, Yokohama, 223-8522, Japan;* orcid.org/0000-0002-4728-9767

Notes

The authors declare no competing financial interests.

ACKNOWLEDGMENT

The work was supported by a Grant-in-Aid for Scientific Research (Nos. JP 19H00888, 17K19105 from the Ministry of Education, Culture, Sports, Science and Technology (MEXT), Japan. YK appreciates fruitful discussions with Prof. Kazuyuki Ishii (The University of Tokyo) and with Prof. Tomoaki Yago (Saitama University) on the importance of the $\boldsymbol{H}_{\mathrm{TTss}}$ interaction included in the spectrum computations. This work was carried out by the joint research program of Molecular Photoscience Research Center, Kobe University.

REFERENCES

(1) Smith, M. B.; Michl, J., Singlet Fission. *Chem. Rev.* **2010**, *110,* 6891-6936.

(2) Shockley, W.; Queisser, H. J., Detailed Balance Limit of Efficiency of P-N Junction Solar Cells. *J. Appl. Phys.* **1961**, *32,* 510-519.

(3) Zang, H.; Zhao, Y.; Liang, W. Z., Quantum Interference in Singlet Fission: J- and H-Aggregate Behavior. *J. Phys. Chem. Lett.* **2017**, *8,* 5105-5112.

(4) Arias, D. H.; Ryerson, J. L.; Cook, J. D.; Damrauer, N. H.; Johnson, J. C., Polymorphism Influences Singlet Fission Rates in Tetracene Thin Films. *Chem. Sci.* **2016**, *7,* 1185-1191.

(5) Zimmerman, P. M.; Zhang, Z. Y.; Musgrave, C. B., Singlet Fission in Pentacene through Multi-Exciton Quantum States. *Nat. Chem.* **2010**, *2,* 648-652.

(6) Johnson, J. C.; Nozik, A. J.; Michl, J., The Role of Chromophore Coupling in Singlet Fission. *Accounts Chem. Res.* **2013**, *46,* 1290-1299.

(7) Zirzlmeier, J.; Lehnherr, D.; Coto, P. B.; Chernick, E. T.; Casillas, R.; Basel, B. S.; Thoss, M.; Tykwinski, R. R.; Guldi, D. M., Singlet Fission in Pentacene Dimers. *Proc. Natl. Acad. Sci. U. S. A.* **2015**, *112,* 5325-5330.

(8) Chan, W.-L.; Berkelbach, T. C.; Provorse, M. R.; Monahan, N. R.; Tritsch, J. R.; Hybertsen, M. S.; Reichman, D. R.; Gao, J.; Zhu, X. Y., The Quantum Coherent Mechanism for Singlet Fission: Experiment and Theory. *Accounts Chem. Res.* **2013**, *46,* 1321-1329.

(9) Miyata, K.; Conrad-Burton, F. S.; Geyer, F. L.; Zhu, X. Y., Triplet Pair States in Singlet Fission. *Chem. Rev.* **2019**, *119,* 4261-4292.

(10) Yamakado, T.; Takahashi, S.; Watanabe, K.; Matsumoto, Y.; Osuka, A.; Saito, S., Conformational Planarization Versus Singlet Fission: Distinct Excited-State Dynamics of Cyclooctatetraene-Fused Acene Dimers. *Angew. Chem.-Int. Edit.* **2018**, *57,* 5438-5443.

(11) Shizu, K.; Adachi, C.; Kaji, H., Effect of Vibronic Coupling on Correlated Triplet Pair Formation in the Singlet Fission Process of Linked Tetracene Dimers. *J. Phys. Chem. A* **2020**, *124,* 3641-3651.

(12) Alvertis, A. M.; Lukman, S.; Hele, T. J. H.; Fuemmeler, E. G.; Feng, J.; Wu, J.; Greenham, N. C.; Chin, A. W.; Musser, A. J., Switching between Coherent and Incoherent Singlet Fission Via Solvent-Induced Symmetry Breaking. *J. Am. Chem. Soc.* **2019**, *141,* 17558-17570.

(13) Fuemmeler, E. G.; Sanders, S. N.; Pun, A. B.; Kumarasamy, E.; Zeng, T.; Miyata, K.; Steigerwald, M. L.; Zhu, X. Y.; Sfeir, M. Y.; Campos, L. M., et al., A Direct Mechanism of Ultrafast Intramolecular Singlet Fission in Pentacene Dimers. *ACS Cent. Sci.* **2016**, *2,* 316-324.

(14) Sanders, S. N.; Kumarasamy, E.; Fallon, K. J.; Sfeir, M. Y.; Campos, L. M., Singlet Fission in a Hexacene Dimer: Energetics Dictate Dynamics. *Chem. Sci.* **2020**, *11,* 1079-1084.

(15) Miyata, K.; Kurashige, Y.; Watanabe, K.; Sugimoto, T.; Takahashi, S.; Tanaka, S.; Takeya, J.; Yanai, T.; Matsumoto, Y., Coherent Singlet Fission Activated by Symmetry Breaking. *Nat. Chem.* **2017**, *9,* 983-989.

(16) Tayebjee, M. J. Y.; Sanders, S. N.; Kumarasamy, E.; Campos, L. M.; Sfeir, M. Y.; McCamey, D. R., Quintet Multiexciton Dynamics in Singlet Fission. *Nat. Phys.* **2017**, *13,* 182-188.

(17) Weiss, L. R.; Bayliss, S. L.; Kraffert, F.; Thorley, K. J.; Anthony, J. E.; Bittl, R.; Friend, R. H.; Rao, A.; Greenham, N. C.; Behrends, J., Strongly Exchange-Coupled Triplet Pairs in an Organic Semiconductor. *Nat. Phys.* **2017**, *13,* 176-181.

(18) Saegusa, T.; Sakai, H.; Nagashima, H.; Kobori, Y.; Tkachenko, N. V.; Hasobe, T., Controlled Orientations of Neighboring Tetracene Units by Mixed Self-Assembled Monolayers

on Gold Nanoclusters for High-Yield and Long-Lived Triplet Excited States through Singlet Fission. *J. Am. Chem. Soc.* **2019**, *141,* 14720-14727.

(19) Lubert-Perquel, D.; Salvadori, E.; Dyson, M.; Stavrinou, P. N.; Montis, R.; Nagashima, H.; Kobori, Y.; Heutz, S.; Kay, C. W. M., Identifying Triplet Pathways in Dilute Pentacene Films. *Nat. Commun.* **2018**, *9,* 4222.

(20) Matsui, Y.; Kawaoka, S.; Nagashima, H.; Nakagawa, T.; Okamura, N.; Ogaki, T.; Ohta, E.; Akimoto, S.; Sato-Tomita, A.; Yagi, S., et al., Exergonic Intramolecular Singlet Fission of an Adamantane-Linked Tetracene Dyad Via Twin Quintet Multiexcitons. *J. Phys. Chem. C* **2019**, *123,* 18813-18823.

(21) Nagashima, H.; Kawaoka, S.; Akimoto, S.; Tachikawa, T.; Matsui, Y.; Ikeda, H.; Kobori, Y., Singlet-Fission-Born Quintet State: Sublevel Selections and Trapping by Multiexciton Thermodynamics. *J. Phys. Chem. Lett.* **2018**, *9,* 5855-5861.

(22) Matsuda, S.; Oyama, S.; Kobori, Y., Electron Spin Polarization Generated by Transport of Singlet and Quintet Multiexcitons to Spin-Correlated Triplet Pairs During Singlet Fissions. *Chem. Sci.* **2020**, *11,* 2934-2942.

(23) Chen, M.; Krzyaniak, M. D.; Nelson, J. N.; Bae, Y. J.; Harvey, S. M.; Schaller, R. D.; Young, R. M.; Wasielewski, M. R., Quintet-Triplet Mixing Determines the Fate of the Multiexciton State Produced by Singlet Fission in a Terrylenediimide Dimer at Room Temperature. *Proc. Natl. Acad. Sci. U. S. A.* **2019**, *116,* 8178-8183.

(24) Bayliss, S. L.; Weiss, L. R.; Kraffert, F.; Granger, D. B.; Anthony, J. E.; Behrends, J.; Bittl, R., Probing the Wave Function and Dynamics of the Quintet Multiexciton State with Coherent Control in a Singlet Fission Material. *Phys. Rev. X* **2020**, *10,* 021070.

(25) Basel, B. S.; Zirzlmeier, J.; Hetzer, C.; Phelan, B. T.; Krzyaniak, M. D.; Reddy, S. R.; Coto, P. B.; Horwitz, N. E.; Young, R. M.; White, F. J., et al., Unified Model for Singlet Fission within a Non-Conjugated Covalent Pentacene Dimer. *Nat. Commun.* **2017**, *8,* 15171.

(26) Sakai, H.; Inaya, R.; Nagashima, H.; Nakamura, S.; Kobori, Y.; Tkachenko, N. V.; Hasobe, T., Multiexciton Dynamics Depending on Intramolecular Orientations in Pentacene Dimers: Recombination and Dissociation of Correlated Triplet Pairs. *J. Phys. Chem. Lett.* **2018**, *9,* 3354-3360.

(27) Collins, M. I.; McCamey, D. P.; Tayebjee, M. J. Y., Fluctuating Exchange Interactions Enable Quintet Multiexciton Formation in Singlet Fission. *J. Chem. Phys.* **2019**, *151,* 164104.

(28) Closs, G. L.; Forbes, M. D. E.; Norris, J. R., Spin-Polarized Electron-Paramagnetic Resonance-Spectra of Radical Pairs in Micelles - Observation of Electron-Spin Spin Interactions. *J. Phys. Chem.* **1987**, *91,* 3592-3599.

(29) Hore, P. J.; Hunter, D. A.; McKie, C. D.; Hoff, A. J., Electron Paramagnetic Resonance of Spin-Correlated Radical Pairs in Photosynthetic Reactions. *Chem. Phys. Lett.* **1987**, *137,* 495-500.

(30) Korovina, N. V.; Chang, C. H.; Johnson, J. C., Spatial Separation of Triplet Excitons Drives Endothermic Singlet Fission. *Nat. Chem.* **2020**, *12,* 391-398.

(31) Tao, G. H., Understanding Electronically Non-Adiabatic Relaxation Dynamics in Singlet Fission. *J. Chem. Theory Comput.* **2015**, *11,* 28-36.

(32) Kobori, Y.; Sekiguchi, S.; Akiyama, K.; Tero-Kubota, S., Chemically Induced Dynamic Electron Polarization Study on the Mechanism of Exchange Interaction in Radical Ion Pairs Generated by Photoinduced Electron Transfer Reactions. *J. Phys. Chem. A* **1999**, *103,* 5416-5424.

(33) Kobori, Y.; Ponomarenko, N.; Norris, J. R., Time-Resolved Electron Paramagnetic Resonance Study on Cofactor Geometries and Electronic Couplings after Primary Charge Separations in the Photosynthetic Reaction Center. *J. Phys. Chem. C* **2015**, *119,* 8078-8088.

(34) Shushin, A. I., The Relaxational Mechanism of Net Cidep Generation in Triplet-Radical Quenching. *Chem. Phys. Lett.* **1993**, *208,* 173-178.

(35) Fukuju, T.; Yashiro, H.; Maeda, K.; Murai, H., Real-Time Observation of the Singlet–Triplet Dephasing Effect on the Spin Dynamics of the Spin-Correlated Radical Pair Formed in the Photolysis of Tetraphenylhydrazine in a Micelle. *Chem. Phys. Lett.* **1999**, *304,* 173-179.

(36) Pensack, R. D.; Ostroumov, E. E.; Tilley, A. J.; Mazza, S.; Grieco, C.; Thorley, K. J.; Asbury, J. B.; Seferos, D. S.; Anthony, J. E.; Scholes, G. D., Observation of Two Triplet-Pair Intermediates in Singlet Exciton Fission. *J. Phys. Chem. Lett.* **2016**, *7,* 2370-2375.

(37) Kobori, Y.; Yago, T.; Akiyama, K.; Tero-Kubota, S.; Sato, H.; Hirata, F.; Norris, J. R., Superexchange Electron Tunneling Mediated by Solvent Molecules: Pulsed Electron Paramagnetic Resonance Study on Electronic Coupling in Solvent-Separated Radical Ion Pairs. *J. Phys. Chem. B* **2004**, *108,* 10226-10240.

(38) Kobori, Y.; Noji, R.; Tsuganezawa, S., Initial Molecular Photocurrent: Nanostructure and Motion of Weakly Bound Charge-Separated State in Organic Photovoltaic Interface. *J. Phys. Chem. C* **2013**, *117,* 1589-1599.

(39) Nakamura, M.; Kishimoto, K.; Kobori, Y.; Abe, T.; Yoza, K.; Kobayashi, K., Self-Assembled Molecular Gear: A 4:1 Complex of Rh(III)Cl Tetraarylporphyrin and Tetra(P-Pyridyl)Cavitand. *J. Am. Chem. Soc.* **2016**, *138,* 12564-12577.

(40) Hoshina, H.; Kanemura, T.; Ruggiero, M. T., Exploring the Dynamics of Bound Water in Nylon Polymers with Terahertz Spectroscopy. *J. Phys. Chem. B* **2020**, *124,* 422-429.

(41) Tsukushi, I.; Yamamuro, O.; Yamamoto, K.; Takeda, K.; Kanaya, T.; Matsuo, T., Neutron Scattering Study of Glassy Toluene: Dynamics of a Quasi-Rigid Molecular Glass. *J. Phys. Chem. Solids* **1999**, *60,* 1541-1543.

(42) Thamarath, S. S.; Bode, B. E.; Prakash, S.; Gupta, K. B. S. S.; Alia, A.; Jeschke, G.; Matysik, J., Electron Spin Density Distribution in the Special Pair Triplet of Rhodobacter Sphaeroides R26 Revealed by Magnetic Field Dependence of the Solid-State Photo-Cidnp Effect. *J. Am. Chem. Soc.* **2012**, *134,* 5921-5930.

(43) Abraham, V.; Mayhall, N. J., Simple Rule to Predict Boundedness of Multiexciton States in Covalently Linked Singlet-Fission Dimers. *J. Phys. Chem. Lett.* **2017**, *8,* 5472-5478.

(44) Wakasa, M.; Yago, T.; Sonoda, Y.; Katoh, R., Structure and Dynamics of Triplet-Exciton Pairs Generated from Singlet Fission Studied Via Magnetic Field Effects. *Commun. Chem.* **2018**, *1,* 9.

(45) Grieco, C.; Kennehan, E. R.; Rimshaw, A.; Payne, M. M.; Anthony, J. E.; Asbury, J. B., Harnessing Molecular Vibrations to Probe Triplet Dynamics During Singlet Fission. *J. Phys. Chem. Lett.* **2017**, *8,* 5700-5706.

TOC graphics

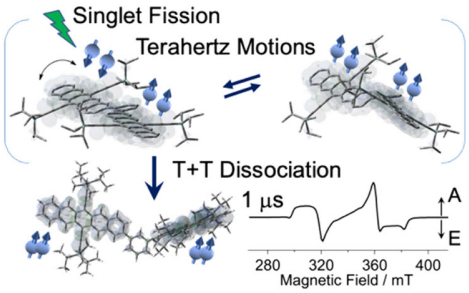

Supporting Information for

Geometries and Terahertz Motions Driving Quintet Multiexcitons and Ultimate Triplet-Triplet Dissociations via the Intramolecular Singlet-Fissions

Yasuhiro Kobori, [†,¢] Masaaki Fuki, [†,¢] Shunta Nakamura,[¶] and Taku Hasobe,[¶]*

[†] Molecular Photoscience Research Center, Kobe University, 1–1 Rokkodai–cho, Nada–ku, Kobe 657–8501, Japan

[¢] Department of Chemistry, Graduate School of Science, Kobe University, 1–1 Rokkodai–cho, Nada–ku, Kobe 657–8501, Japan

[¶] Department of Chemistry, Faculty of Science and Technology, Keio University, Yokohama, 223-8522, Japan

[*] Corresponding Author: Phone: +81-78-803-6548; E-mail: ykobori@kitty.kobe-u.ac.jp

Electron spin polarization transfer model with considering the molecular motions in the TT and T+T states in the multiexciton

From Figure 4 and eqs.(2)-(4) in the main text, the following coupled stochastic-Liouville equation can be obtained in the ${}^5(\mathrm{TT})_{m_\mathrm{S}} - {}^1(\mathrm{TT})$ two-level systems where m_S = +2, +1, 0, -1 and -2, assuming that the quintet-triplet and the singlet-triplet interconversions are ignored.

$$\dot{\boldsymbol{\rho}}_{\mathrm{TT1}} = -i\left[\begin{pmatrix} E^{\mathrm{TT1}}_{\mathrm{Q}_{m_\mathrm{S}}} & 0 \\ 0 & E^{\mathrm{TT1}}_{\mathrm{S}} \end{pmatrix}, \boldsymbol{\rho}_{\mathrm{TT1}}\right] - k_{12}\boldsymbol{\rho}_{\mathrm{TT1}} + k_{12}\boldsymbol{\rho}_{\mathrm{TT2}} - k_{\mathrm{DISS}}\boldsymbol{\rho}_{\mathrm{TT1}} - \begin{pmatrix} 0 & k_{\mathrm{REC}}\rho^{\mathrm{TT1}}_{\mathrm{Q}_{m_\mathrm{S}}\mathrm{S}}/2 \\ k_{\mathrm{REC}}\rho^{\mathrm{TT1}}_{\mathrm{SQ}_{m_\mathrm{S}}}/2 & k_{\mathrm{REC}}\rho^{\mathrm{TT1}}_{\mathrm{SS}} \end{pmatrix} \tag{S1}$$

$$\dot{\boldsymbol{\rho}}_{\mathrm{TT2}} = -i\left[\begin{pmatrix} H^{\mathrm{TT2}}_{\mathrm{Q}_{m_\mathrm{S}}\mathrm{Q}_{m_\mathrm{S}}} & H^{\mathrm{TT2}}_{\mathrm{Q}_{m_\mathrm{S}}\mathrm{S}} \\ H^{\mathrm{TT2}}_{\mathrm{SQ}_{m_\mathrm{S}}} & H^{\mathrm{TT2}}_{\mathrm{SS}} \end{pmatrix}, \boldsymbol{\rho}_{\mathrm{TT2}}\right] + k_{12}\boldsymbol{\rho}_{\mathrm{TT1}} - k_{12}\boldsymbol{\rho}_{\mathrm{TT2}} \tag{S2}$$

$$\dot{\boldsymbol{\rho}}_{\mathrm{T+T}} = -i\left[\begin{pmatrix} H^{\mathrm{T+T}}_{\mathrm{Q}_{m_\mathrm{S}}\mathrm{Q}_{m_\mathrm{S}}} & H^{\mathrm{T+T}}_{\mathrm{Q}_{m_\mathrm{S}}\mathrm{S}} \\ H^{\mathrm{T+T}}_{\mathrm{SQ}_{m_\mathrm{S}}} & H^{\mathrm{T+T}}_{\mathrm{SS}} \end{pmatrix}, \boldsymbol{\rho}_{\mathrm{T+T}}\right] + k_{\mathrm{DISS}}\boldsymbol{\rho}_{\mathrm{TT1}} - \begin{pmatrix} 0 & k_2\rho^{\mathrm{T+T}}_{\mathrm{Q}_{m_\mathrm{S}}\mathrm{S}}/2 \\ k_2\rho^{\mathrm{T+T}}_{\mathrm{SQ}_{m_\mathrm{S}}}/2 & k_2\rho^{\mathrm{TT1}}_{\mathrm{SS}} \end{pmatrix} \tag{S3}$$

where superscripts represent the strongly-coupled TT1 site with large J_1, the thermally activated TT2 site with the intermediate coupling of $J_2 \approx$ -10 GHz, and the de-coupled T+T site, respectively. $E^{\mathrm{TT1}}_{\mathrm{Q}_{m_\mathrm{S}}}$ and $E^{\mathrm{TT1}}_{\mathrm{S}}$ are the eigenenegies in TT_1. In the subscripts, ${}^5(\mathrm{TT})_{m_\mathrm{S}} = \mathrm{Q}_{m_\mathrm{S}}$ and ${}^1(\mathrm{TT}) = \mathrm{S}$ are attributable. $H_{\mathrm{Q}_{m_\mathrm{S}}\mathrm{Q}_{m_\mathrm{S}}}$, $H_{\mathrm{Q}_{m_\mathrm{S}}\mathrm{S}}$, $H_{\mathrm{SQ}_{m_\mathrm{S}}}$ and H_{SS} are respective diagonal and off-diagonal terms of the spin Hamiltonians ($\boldsymbol{H}_{\mathrm{TT2}}$, and $\boldsymbol{H}_{\mathrm{T+T}}$) on the basis spin system of ${}^5(\mathrm{TT})_{m_\mathrm{S}}$ and ${}^1(\mathrm{TT})$ in the TT_1 state. The density matrices are thus represented for the ${}^5(\mathrm{TT})_{m_\mathrm{S}} - {}^1(\mathrm{TT})$ two-level systems, as, follows.

$$\boldsymbol{\rho}_{\mathrm{TT1}} = \begin{pmatrix} \rho^{\mathrm{TT1}}_{\mathrm{Q}_{m_\mathrm{S}}\mathrm{Q}_{m_\mathrm{S}}} & \rho^{\mathrm{TT1}}_{\mathrm{Q}_{m_\mathrm{S}}\mathrm{S}} \\ \rho^{\mathrm{TT1}}_{\mathrm{SQ}_{m_\mathrm{S}}} & \rho^{\mathrm{TT1}}_{\mathrm{SS}} \end{pmatrix} \tag{S4}$$

$$\boldsymbol{\rho}_{\mathrm{TT2}} = \begin{pmatrix} \rho^{\mathrm{TT2}}_{\mathrm{Q}_{m_\mathrm{S}}\mathrm{Q}_{m_\mathrm{S}}} & \rho^{\mathrm{TT2}}_{\mathrm{Q}_{m_\mathrm{S}}\mathrm{S}} \\ \rho^{\mathrm{TT2}}_{\mathrm{SQ}_{m_\mathrm{S}}} & \rho^{\mathrm{TT2}}_{\mathrm{SS}} \end{pmatrix} \tag{S5}$$

$$\boldsymbol{\rho}_{\mathrm{T+T}} = \begin{pmatrix} \rho^{\mathrm{T+T}}_{\mathrm{Q}m_{\mathrm{S}}\mathrm{Q}m_{\mathrm{S}}} & \rho^{\mathrm{T+T}}_{\mathrm{Q}m_{\mathrm{S}}\mathrm{S}} \\ \rho^{\mathrm{T+T}}_{\mathrm{SQ}m_{\mathrm{S}}} & \rho^{\mathrm{T+T}}_{\mathrm{SS}} \end{pmatrix} \qquad \text{(S6)}$$

Coupled time-differential equations in the twelve elements in eqs. (S4)-(S6) are described by regenerating a $\vec{\boldsymbol{\rho}}$ vector composed of these elements. Then, the following master equation is obtained:

$$\frac{\partial \vec{\boldsymbol{\rho}}}{\partial t} = \boldsymbol{L}\vec{\boldsymbol{\rho}} \qquad \text{(S7)}$$

where $\boldsymbol{L}$ is summarized in Table S1. In this table, $\rho_{\mathrm{QQ1}} = \rho^{\mathrm{TT1}}_{\mathrm{Q}m_{\mathrm{S}}\mathrm{Q}m_{\mathrm{S}}}$, $\rho_{\mathrm{QS1}} = \rho^{\mathrm{TT1}}_{\mathrm{Q}m_{\mathrm{S}}\mathrm{S}}$, $\rho_{\mathrm{SQ1}} = \rho^{\mathrm{TT1}}_{\mathrm{SQ}m_{\mathrm{S}}}$, $\rho_{\mathrm{SS1}} = \rho^{\mathrm{TT1}}_{\mathrm{SS}}$, $\rho_{\mathrm{QQ2}} = \rho^{\mathrm{TT2}}_{\mathrm{Q}m_{\mathrm{S}}\mathrm{Q}m_{\mathrm{S}}}$, $\rho_{\mathrm{QS2}} = \rho^{\mathrm{TT2}}_{\mathrm{Q}m_{\mathrm{S}}\mathrm{S}}$, $\rho_{\mathrm{SQ2}} = \rho^{\mathrm{TT2}}_{\mathrm{SQ}m_{\mathrm{S}}}$, $\rho_{\mathrm{SS2}} = \rho^{\mathrm{TT2}}_{\mathrm{SS}}$, $\rho_{\mathrm{QQ(T+T)}} = \rho^{\mathrm{T+T}}_{\mathrm{Q}m_{\mathrm{S}}\mathrm{Q}m_{\mathrm{S}}}$, $\rho_{\mathrm{QS(T+T)}} = \rho^{\mathrm{T+T}}_{\mathrm{Q}m_{\mathrm{S}}\mathrm{S}}$, $\rho_{\mathrm{SQ(T+T)}} = \rho^{\mathrm{T+T}}_{\mathrm{SQ}m_{\mathrm{S}}}$, $\rho_{\mathrm{SS(T+T)}} = \rho^{\mathrm{T+T}}_{\mathrm{SS}}$ are attributable in eqs.(S4)-(S6).

From eq.(9) and eq.(S3), the nine spin-state populations ($\boldsymbol{\rho}^{\mathrm{T+T}_{\mathrm{ii}}}$) where i = 1, 2, ⋯, 9 in the dissociated multiexciton is obtained from the diagonal terms in $\boldsymbol{\rho}^{\mathrm{T+T}}_{1-9} = \boldsymbol{U}^{t}_{\mathrm{T+T}}\boldsymbol{\rho}^{\mathrm{T+T}}\boldsymbol{U}_{\mathrm{T+T}}$, where,

$$\boldsymbol{\rho}^{\mathrm{T+T}} = \begin{pmatrix} \ddots & & & & & \vdots \\ & \rho^{\mathrm{T+T}}_{\mathrm{Q}m_{\mathrm{S}}\mathrm{Q}m_{\mathrm{S}}} & & \cdots & & \rho^{\mathrm{T+T}}_{\mathrm{Q}m_{\mathrm{S}}\mathrm{S}} \\ & & \ddots & & & \vdots \\ & & & 0 & & \\ & \vdots & & & 0 & \vdots \\ & & & & & 0 \\ \cdots & \rho^{\mathrm{T+T}}_{\mathrm{SQ}m_{\mathrm{S}}} & \cdots & & \cdots & \sum_{m_{\mathrm{S}}} \rho^{\mathrm{T+T}}_{\mathrm{SS}}/5 \end{pmatrix} \qquad \text{(S8)}$$

Table S1. Matrix elements of $\boldsymbol{L}$ in $\partial\vec{\boldsymbol{\rho}}/\partial t = \boldsymbol{L\rho}$ described in the basis spin system of $\widehat{\boldsymbol{H}}_{\mathrm{TT1}}$.[a)]

ρ_{QQ1}	$-k_{12}-k_{\mathrm{DISS}}$				k_{21}							
ρ_{QS1}		$-k_{12}-k_{\mathrm{DISS}}-k_{\mathrm{REC}}/2$ $-i(E^{\mathrm{TT1}}_{\mathrm{Q}m_{\mathrm{S}}}-E^{\mathrm{TT1}}_{\mathrm{S}})$				k_{21}						
ρ_{SQ1}			$-k_{12}-k_{\mathrm{DISS}}-k_{\mathrm{REC}}/2$ $+i(E^{\mathrm{TT1}}_{\mathrm{Q}m_{\mathrm{S}}}-E^{\mathrm{TT1}}_{\mathrm{S}})$				k_{21}					
ρ_{SS1}				$-k_{12}$ $-k_{\mathrm{DISS}}-k_{\mathrm{REC}}$				k_{21}				
ρ_{QQ2}	k_{12}				$-k_{21}$	$iH^{\mathrm{TT2}}_{\mathrm{SQ}m_{\mathrm{S}}}$	$-iH^{\mathrm{TT2}}_{\mathrm{Q}m_{\mathrm{S}}\mathrm{S}}$					
ρ_{QS2}		k_{12}			$iH^{\mathrm{TT2}}_{\mathrm{Q}m_{\mathrm{S}}\mathrm{S}}$	$-i(H^{\mathrm{TT2}}_{\mathrm{Q}m_{\mathrm{S}}\mathrm{Q}m_{\mathrm{S}}}-H^{\mathrm{TT2}}_{\mathrm{SS}})-k_{21}$		$-iH^{\mathrm{TT2}}_{\mathrm{Q}m_{\mathrm{S}}\mathrm{S}}$				
ρ_{SQ2}			k_{12}		$-iH^{\mathrm{TT2}}_{\mathrm{SQ}m_{\mathrm{S}}}$		$i(H^{\mathrm{TT2}}_{\mathrm{Q}m_{\mathrm{S}}\mathrm{Q}m_{\mathrm{S}}}-$ $H^{\mathrm{TT2}}_{\mathrm{SS}})-k_{21}$	$iH^{\mathrm{TT2}}_{\mathrm{SQ}m_{\mathrm{S}}}$				
ρ_{SS2}				k_{12}		$-iH^{\mathrm{TT2}}_{\mathrm{SQ}m_{\mathrm{S}}}$	$iH^{\mathrm{TT2}}_{\mathrm{Q}m_{\mathrm{S}}\mathrm{S}}$	$-k_{21}$				
$\rho_{\mathrm{QQ(T+T)}}$	k_{DISS}									$iH^{\mathrm{T+T}}_{\mathrm{SQ}m_{\mathrm{S}}}$	$-iH^{\mathrm{T+T}}_{\mathrm{Q}m_{\mathrm{S}}\mathrm{S}}$	
$\rho_{\mathrm{QS(T+T)}}$		k_{DISS}							$iH^{T+T}_{\mathrm{Q}m_{\mathrm{S}}\mathrm{S}}$	$-i(H^{\mathrm{T+T}}_{\mathrm{Q}m_{\mathrm{S}}\mathrm{Q}m_{\mathrm{S}}}-$ $H^{\mathrm{T+T}}_{SS})-k_2/2$		$-iH^{\mathrm{T+T}}_{\mathrm{Q}m_{\mathrm{S}}\mathrm{S}}$
$\rho_{\mathrm{SQ(T+T)}}$			k_{DISS}						$-iH^{\mathrm{T+T}}_{\mathrm{SQ}m_{\mathrm{S}}}$		$i(H^{\mathrm{T+T}}_{\mathrm{Q}m_{\mathrm{S}}\mathrm{Q}m_{\mathrm{S}}}-$ $H^{\mathrm{T+T}}_{\mathrm{SS}})-k_2/2$	$iH^{\mathrm{T+T}}_{\mathrm{SQ}m_{\mathrm{S}}}$
$\rho_{\mathrm{SS(T+T)}}$				k_{DISS}						$-iH^{\mathrm{T+T}}_{\mathrm{SQ}m_{\mathrm{S}}}$	$iH^{\mathrm{T+T}}_{\mathrm{Q}m_{\mathrm{S}}\mathrm{S}}$	$-k_2$

[a)] To treat the ESPT in eqs.(2)-(4), one needs to obtain all of the density matrix elements computed under one basis spin system composed of quintet, triplet and singlet TT for the TT_1, TT_2, and T+T states. In Table S1, we chose the basis set obtained by diagonalizing the spin Hamiltonian of $\widehat{\boldsymbol{H}}_{\mathrm{TT1}}$.

Table S2. Parameters applied for computations of the delay time dependence of the EPR spectra (Figure 2) in PcD at 77 K in toluene.

State		J /MHz	D /MHz [a)]	E /MHz [a)]	D_{SS} / MHz	Euler angles [b)] / degrees (α, β, γ)	Dipolar angles [c)]/ degrees	$\bar{\nu}_{vib}$/ cm^{-1}	k_{DISS} / s^{-1}	k_{REC} / s^{-1} (Singlet recombination)
o-(Pc)$_2$	TT_1	-2.2×10^5	1,060	-37	-120	α = -10 β = 30 γ = 120	θ_2 =40 ϕ_2 =120	26	1.1×10^6	2.0×10^7
	TT_2	-8.4×10^3	1,060	-37	-120	α = -15 β = 53 γ = 120	θ_2 =40 ϕ_2 =120			-
	T+T	-8.4	1,130	-40	-80	α = -70 β = 60 γ = 110	θ_2 =25 ϕ_2 =170	-		k_2 = 9.0×10^6
m-(Pc)$_2$	TT_1	-9.8×10^4	1,090	-17	-120	α = 20 β = 22 γ = 10	θ_2 =70 ϕ_2 =160	72	1.0×10^6	3.0×10^6
	TT_2	-1.4×10^4	1,090	-17	-120	α = 20 β = 75 γ = 20	θ_2 =70 ϕ_2 =160			-
	T+T	-4.2	1,200	-19	-30	α = -100 β = 90 γ = -70	θ_2 =81 ϕ_2 =170	-		k_2 = 1.0×10^6

[a)] Zero-field splitting parameters in $\boldsymbol{H}_{zfs} = D\{S_z^2 - S(S+1)/3\} + E\left(S_x^2 - S_y^2\right)$ for each triplet in the multiexciton.

[b)] Conformation of the principal axes of the T_B component with respect to the principal axes of T_A component in Figure 3, 5 and 6.

[c)] Direction for the T_B component was set by the polar angles (θ_2 and ϕ_2) with respect the (X_1, Y_1, Z_1) principal axes in T_A.

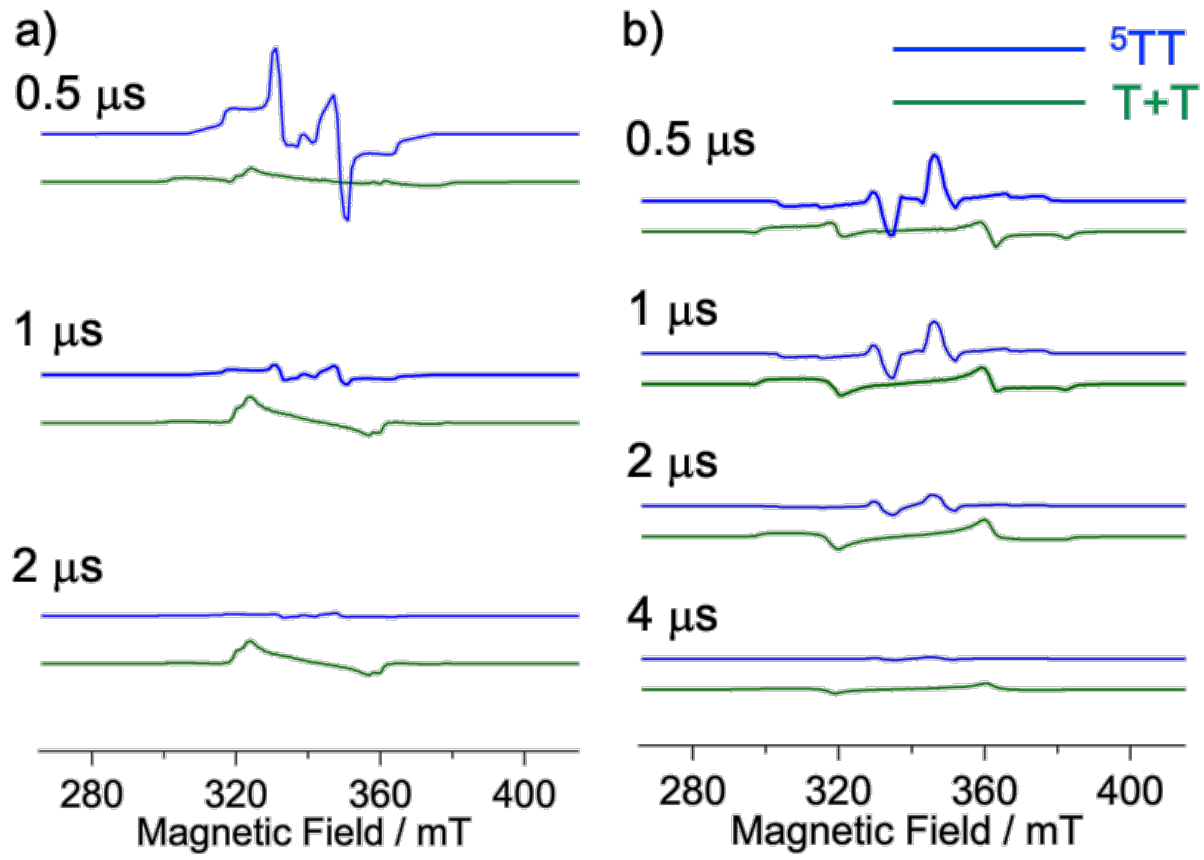

Figure S1. Computed delay time dependences of the transvers magnetizations of the quintet state ($^5TT_1$ + $^5TT_2$) and the dissociated intramolecular T+T states in a) *o*-$(Pc)_2$ and in b) *m*-$(Pc)_2$, respectively, from eq.(13). Summations of the blue and green lines are shown by the red lines in Figure 2.

Table S3. Matrix elements of the magnitudes of the spin Hamiltonian [abs($\boldsymbol{H}_{\mathrm{TT2}}$)] calculated for the TT_2 state with the $\boldsymbol{B}_0$ direction of (θ, ϕ) = (90°,43°) in the (X_1, Y_1, Z_1) coordinate in *m*-$(Pc)_2$ in the unit of rad/s.[a)]

	Q_2	Q_1	Q_0	Q_{-1}	Q_{-2}	T_1	T_0	T_{-1}	S
Q_2	2.94193e+11	9.64045e+08	2.0559e+09	4.73919e+07	7.0842e+06	1.12781e+09	4.11416e+09	1.029e+06	**6.47884e+08**
Q_1	9.64045e+08	2.3671e+11	4.16411e+08	2.49372e+09	4.9663e+07	5.47587e+08	7.89388e+08	2.90769e+09	**1.43317e+09**
Q_0	2.0559e+09	4.16411e+08	1.77709e+11	3.79008e+08	2.02062e+09	1.38869e+09	1.43685e+08	1.37238e+09	**2.28222e+09**
Q_{-1}	4.73919e+07	2.49372e+09	3.79008e+08	1.17081e+11	9.78508e+08	2.96406e+09	8.02598e+08	7.96413e+08	**1.37233e+09**
Q_{-2}	7.0842e+06	4.9663e+07	2.02062e+09	9.78508e+08	5.4755e+10	1.0299e+06	4.19404e+09	1.13074e+09	**8.02506e+08**
T_1	1.12781e+09	5.47587e+08	1.38869e+09	2.96406e+09	1.0299e+06	1.15223e+11	6.7911e+08	2.49359e+09	1.35827e+06
T_0	4.11416e+09	7.89388e+08	1.43685e+08	8.02598e+08	4.19404e+09	6.7911e+08	1.78164e+11	6.9791e+08	4.70522e+06
T_{-1}	1.029e+06	2.90769e+09	1.37238e+09	7.96413e+08	1.13074e+09	2.49359e+09	6.9791e+08	2.34882e+11	1.64535e+06
S	**6.47884e+08**	**1.43317e+09**	**2.28222e+09**	**1.37233e+09**	**8.02506e+08**	1.35827e+06	4.70522e+06	1.64535e+06	3.52179e+11

a) S = ^{1}TT , T = ^{3}TT and Q = ^{5}TT . The sizes of the interactions of $\langle Q_2|\boldsymbol{H}_{\mathrm{TT2}}|S\rangle, \langle Q_1|\boldsymbol{H}_{\mathrm{TT2}}|S\rangle, \langle Q_0|\boldsymbol{H}_{\mathrm{TT2}}|S\rangle, \langle Q_{-1}|\boldsymbol{H}_{\mathrm{TT2}}|S\rangle$ and $\langle Q_{-2}|\boldsymbol{H}_{\mathrm{TT2}}|S\rangle$) are shown by the bold characters. The diagonal elements of $\langle T_1|\boldsymbol{H}_{\mathrm{TT2}}|T_1\rangle$, $\langle T_0|\boldsymbol{H}_{\mathrm{TT2}}|T_0\rangle$, $\langle T_{-1}|\boldsymbol{H}_{\mathrm{TT2}}|T_{-1}\rangle$ and $\langle S|\boldsymbol{H}_{\mathrm{TT2}}|S\rangle$ are negative, while the absolute values are positive in this table.

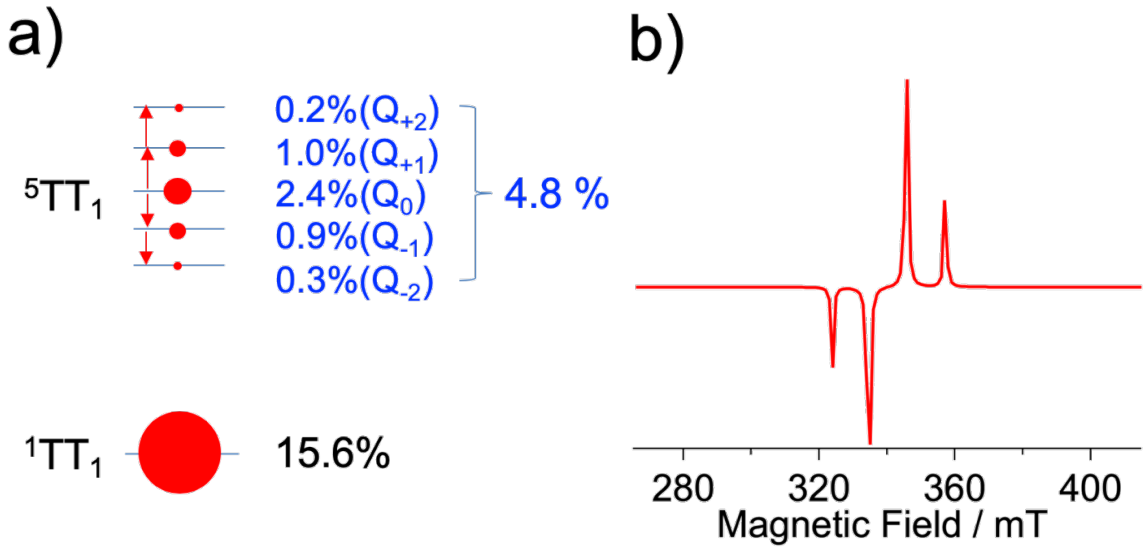

Figure S2. a) Sublevel populations of the strongly coupled multiexciton with the $\boldsymbol{B}_0$ direction of (θ, ϕ) = (90°,43°) in the (X_1, Y_1, Z_1) coordinate in *m*-$(Pc)_2$ calculated at t = 0.5 μs with $\widehat{\boldsymbol{H}}_{TT2}$ in Table S3. Quintet sublevel populations are proportional to are proportional to $\langle {}^5TT_{m_S}|\boldsymbol{H}_{TT2}|\,{}^1TT\rangle^2$ in Table S3 caused by $\boldsymbol{H}_{TTzfs}$. It is noted that the significant amount of the quintet population (4.8 %) occurs from the singlet TT_1 (15.6%) by the anisotropic spin-relaxation effects, although the singlet-quintet gaps are larger than the sizes of $\boldsymbol{H}_{TTzfs}$. The sizes of the spin magnetizations ($\rho_{00} - \rho_{\pm1\pm1}$) larger than 1.4 % for the Q0– Q±1 transitions are greater than the thermal equilibrium spin magnetization of $g\beta B_0/2k_BT = 0.0028$, denoting that the ESP is detectable by the TREPR method. The other populations (79.6 %) occurred at the ground state (S_0S_0:54.9%) and the TT_2 states (2.8%) and T+T states (21.9%). c) EPR spectrum for the $\boldsymbol{B}_0$ direction of (θ, ϕ) = (90°,43°) computed using the populations in a). The four E/E/A/A transition lines corresponds to the four arrows in a).